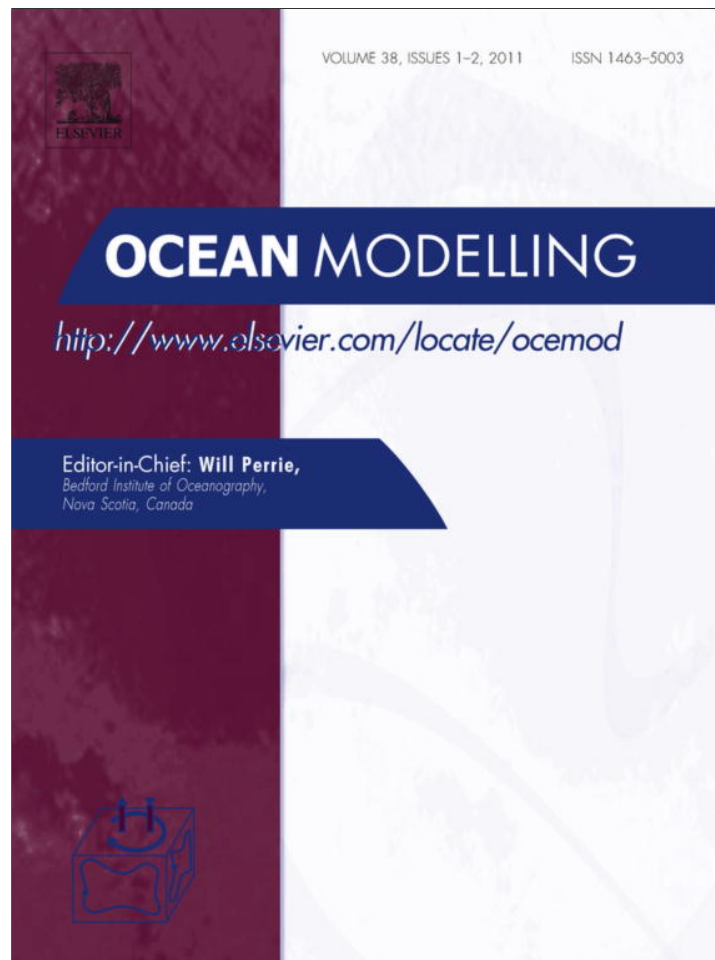


Provided for non-commercial research and education use.
Not for reproduction, distribution or commercial use.



This article appeared in a journal published by Elsevier. The attached copy is furnished to the author for internal non-commercial research and education use, including for instruction at the authors institution and sharing with colleagues.

Other uses, including reproduction and distribution, or selling or licensing copies, or posting to personal, institutional or third party websites are prohibited.

In most cases authors are permitted to post their version of the article (e.g. in Word or Tex form) to their personal website or institutional repository. Authors requiring further information regarding Elsevier's archiving and manuscript policies are encouraged to visit:

<http://www.elsevier.com/copyright>



Contents lists available at ScienceDirect

Ocean Modelling

journal homepage: www.elsevier.com/locate/ocemod

Dynamics of a dense gravity current flowing over a corrugation

Mehmet Ilıcak^{a,*}, Sonya Legg^a, Alistair Adcroft^a, Robert Hallberg^b^a Atmospheric and Oceanic Sciences Program, Princeton University, Princeton, NJ 08540, USA^b NOAA-GFDL, Princeton University, Forrestal Campus, U.S. Route 1, P.O. Box 308, Princeton, NJ 08542, USA

ARTICLE INFO

Article history:

Received 6 October 2010

Received in revised form 20 January 2011

Accepted 13 February 2011

Available online 2 March 2011

Keywords:

Overflow

Mixing

Canyon

Ridge

Gravity current

ABSTRACT

In this study, we investigate the dynamics of a dense gravity currents over different sizes of ridges and canyons. We employ a high resolution idealized isopycnal model and perform a large number of experiments changing the aspect ratio of a ridge/canyon, the Coriolis parameter, the reduced gravity, the background slope and initial overflow thickness. The control run (smooth topography) is in an eddy-regime and the frequencies of the eddies coincide with those of the Filchner overflow (Darelius et al., 2009). Our idealized corrugation experiments show that corrugations steer the plume downslope, and that ridges are more effective than canyons in transporting the overflow to the deep ocean. We find that a corrugation Burger number (Bu_c) can be used as a parameter to describe the flow over topography. Bu_c is a combination of a Froude number and the aspect ratio. The maximum downslope transport of a corrugation can be increased when the height of the corrugation increases (Bu_c increases) or when the width of the corrugation decreases (Bu_c increases).

In addition, we propose a new parameterization of mixing as a function of Bu_c that can be used to account for unresolved shear in coarse resolution models. The new parameterization captures the increased local shear, thus increasing the turbulent kinetic energy and decreasing the gradient Richardson number. We find reasonable agreement in the overflow thickness and transport between the models with this parameterization and the high resolution models. We conclude that mixing effects of corrugations can be implemented as unresolved shear in an eddy diffusivity formulation and this parameterization can be used in coarse resolution models.

© 2011 Elsevier Ltd. All rights reserved.

1. Introduction

Deep and intermediate water formation is crucial for the large scale ocean circulation and plays an important role for the meridional overturning circulation. These dense waters originate in marginal seas and form overflows that flow out through narrow channels and settle in the open ocean at levels determined by entrainment. Important examples of overflows are the Weddell Sea (Foldvik et al., 2004), Ross Sea (Gordon et al., 2004), Denmark Strait (Macrander et al., 2007), Faroe Bank Channel (Mauritzen et al., 2005), Mediterranean Sea (Baringer and Price, 1997) and Red Sea (Peters et al., 2005) overflows. Observations show that only Antarctic overflows sink to the bottom of the ocean while other overflows equilibrate at intermediate depths.

Overflows are bottom-trapped gravity currents and are therefore controlled by the topography (Özgökmen et al., 2004; Ilıcak et al., 2008a). In general, the continental slopes are not smooth and consist of many ridges, canyons and topographic corrugations.

The steering of dense gravity currents by corrugations has been observed in oceanic overflows. Sherwin et al. (2008) describe that a significant part of the Faroe-Shetland Channel Bottom Water appears to be channelled through a canyon that leads southward down the southern flank of the Faroe Bank into the Ellett gully. Foldvik et al. (2004) show that the Weddell Sea overflow is directed by two ridges to the deeper ocean after it leaves the continental shelf and is influenced by planetary rotation. Muench et al. (2009b) suggest that corrugations at the Drygalski Trough in the Ross Sea might be responsible for the enhanced downslope overflow transport that feeds Antarctic Bottom Water (AABW), the dominant abyssal water mass in the world (Johnson, 2008).

There are several approaches to investigate the effects of ridges and canyons on gravity currents. The first is to conduct laboratory experiments (Davies et al., 2006; Darelius, 2008; Wahlin et al., 2008). Their main advantage is that large ensembles of experiments can be performed with known parameters and real fluid. Davies et al. (2006) perform idealized rotating fluid tank experiments to replicate and quantify the main structures of the steady Faroe Bank Channel overflow which flows in a divergent canyon. Darelius (2008) shows that laminar, dense gravity currents are steered downslope by V-shaped ridges and canyons. She observes that the corrugations can transport all the overflow water

* Corresponding author. Address: 201, Forrestal Road, Princeton, 08540 NJ, USA. Tel.: +1 786 3251094.

E-mail addresses: mehmet.ilicak@noaa.gov, milicak@rsmas.miami.edu (M. Ilıcak).

downslope when the transport of the overflow is less than the maximum corrugation transport defined by an analytical theory. Wahlin et al. (2008) perform a set of laboratory experiments in a rotating tank to investigate the effect of small-scale topography on plume mixing. They also find that the dense overflow is directed downslope when a ridge or canyon is present. The total mixing and the entrainment rate of the overflow increases when the flow meets an obstacle (Wahlin et al., 2008). However, the disadvantages of laboratory experiments are that the effective Reynolds number is orders of magnitude smaller (Darelius, 2008) and the topographic slopes are typically much larger than those in the ocean (Wahlin et al., 2008).

An alternative approach to investigating the effects of corrugations on overflows is with high resolution numerical simulations (Jiang and Garwood, 1998; Özgökmen and Fischer, 2008; Wilchinsky and Feltham, 2009; Wang et al., 2009). The Filchner overflow in the Weddell Sea is modeled by Wilchinsky and Feltham (2009) and Wang et al. (2009). The former found that the plume of Ice Shelf Water runs into two ridges when it travels along the slope of the continental shelf. They argue that the temporal variability of the overflow observed by Darelius et al. (2009) can be due to the dome-like structures of the plume. Wilchinsky and Feltham (2009) employ numerical simulations with and without the ridges and find that their presence strongly affects the plume shape. Wang et al. (2009) perform numerical simulations for the Weddell Sea overflow. They find that the eddies formed by the overflow have typical scales of 20–40 km, and a temporal scale of about 3 days. They also show that two ridges shape the details of the overflow structure. Ridges not only split and steer the overflow but also generate strong mixing. Matsumura and Hasumi (2010) also conduct realistic numerical simulations to study the effect of the ridges on Weddell Sea overflow. They find that ridges have two different mechanisms of inducing offshore transport: a strong downslope current at the upstream side of the ridge and offshore transport by eddies that are induced when the overflow passes over the ridge. Numerical simulations in Muench et al. (2009b) suggest that the Ross Sea overflow might be directed downslope by multiple fine scale corrugations ($Height \sim 10 - 100$ m with $Wavelength \sim 1$ km).

Observations and numerical studies therefore show that two well-known deep water formation sites (Ross Sea and Weddell Sea overflows) are influenced by the effect of corrugations. However, the small-scale nature of these corrugations prevents their explicit resolution in global ocean general circulation models (OGCMs) used in climate models. Typically, OGCMs have a resolution of $1^\circ \approx 100$ km in the horizontal direction, which is much larger than the length-scale of the corrugations. Thus, the effect of the corrugations has to be parameterized. In this study, we study the interaction between a single corrugation (canyon or ridge) and a gravity current. Our main goal is to address the following questions:

- How is the dense water transported and mixed over a corrugation?
- Is there a single parameter that describes the flow for different corrugations?
- Can we develop a parameterization of the effects of the corrugation on the overflow for use in OGCMs?

To investigate the effects of a corrugation, we systematically perform idealized experiments with different aspect ratios of the corrugation. Our focus is on the pathway of the overflow in the presence of a canyon or a ridge. The overflow transport and mixing in different simulations are computed for quantitative comparison. We also propose a new numerical parameterization based on physical properties to reproduce the effect of a corrugation in a coarse

model. To our knowledge, this is the first time that a set of detailed and systematic numerical simulations have been conducted to understand the interaction between the overflow and a single corrugation.

Our main findings are the following. Ridges steer the overflow plume off-shore more effectively than canyons with the same aspect ratio. When the height (width) of the obstacle increases, the downslope transport of the plume increases (decreases). This is consistent with the analytical theory developed by Wahlin (2002). We find that the corrugation Burger number (Bu_c) can be used to define the flow over rough topography. We also propose a new parameterization as a function of Bu_c that can be used to represent the effect of unresolved shear on mixing in coarse resolution models. There is a reasonable agreement in the overflow thickness and transport between the coarse models with parameterization and the high resolution models without the parameterization. The outline of this paper is as follows: The numerical model and setup of the experiments are introduced in Section 2. The main results are presented and discussed in Section 3, then we summarize and conclude in Section 4.

2. Model setup

In this study, the Generalized Ocean Layer Dynamics (GOLD) model is employed. GOLD is a free-surface, hydrostatic, primitive equation ocean model that uses isopycnal (density) coordinates in the vertical (Adcroft et al., 2008; Hallberg and Adcroft, 2009; Gnanadesikan and Anderson, 2009). The most obvious advantage of an isopycnal model is that there is no spurious mixing due to the advection schemes in rough topographies unlike in geopotential and terrain-following coordinates (Griffies et al., 2000). Density models have to parameterize the diapycnal mixing explicitly. Here, GOLD uses a new parameterization for bottom boundary and shear induced mixing depending on the local balance of turbulent kinetic energy and shear (Jackson et al., 2008). In this shear-driven parameterization the eddy diffusivity (κ) is computed as

$$\frac{\partial^2 \kappa}{\partial z^2} - \frac{\kappa}{L_d^2} = -2SF(Ri), \quad (1)$$

where S is the vertical shear and L_d is a vertical decay length scale defined as $L_d = 0.82L_b$. Here, $L_b = \sqrt{k}/N$ is the buoyancy length scale where k is the turbulent kinetic energy. The function ($F(Ri)$) on the right hand side of Eq. (1) is the mixing function and depends on the gradient Richardson number, Ri , as

$$F(Ri) = F_o \max\left(0, \frac{1 - Ri/Ri_c}{1 + \alpha Ri/Ri_c}\right). \quad (2)$$

Note that for this parameterization to be effective, the shear causing the mixing must be explicitly resolved. In this study, $\alpha = -0.97$ and $Ri_c = 0.25$, as calibrated against 3D direct numerical simulations of stratified shear instability by Jackson et al. (2008).

The computational domain is similar to the Dynamics of Overflow Mixing and Entrainment (DOME) setup (Legg et al., 2006) but with a negative Coriolis parameter appropriate to the Southern Hemisphere. The domain is 150 km long in the x -direction and 85 km wide in the cross-slope y -direction (Fig. 1(a)). A dense inflow is injected into the northern end of a flat-bottom channel of depth 600 m, width 10 km and 2 km long. The horizontal resolution of 500 m is smaller than the Rossby deformation radius ($L_{RD} \approx 3 - 4$ km). All experiments use 25 isopycnal layers. A single corrugation (ridge or canyon) is placed 35 km east of the opening of the channel (Fig. 1(b)), so that when the overflow encounters the corrugation, the flow is already geostrophically adjusted (recall $f < 0$). The channel opens into an idealized open ocean with a uniform slope, $s = 0.08$, and a maximum depth of 7000 m. The

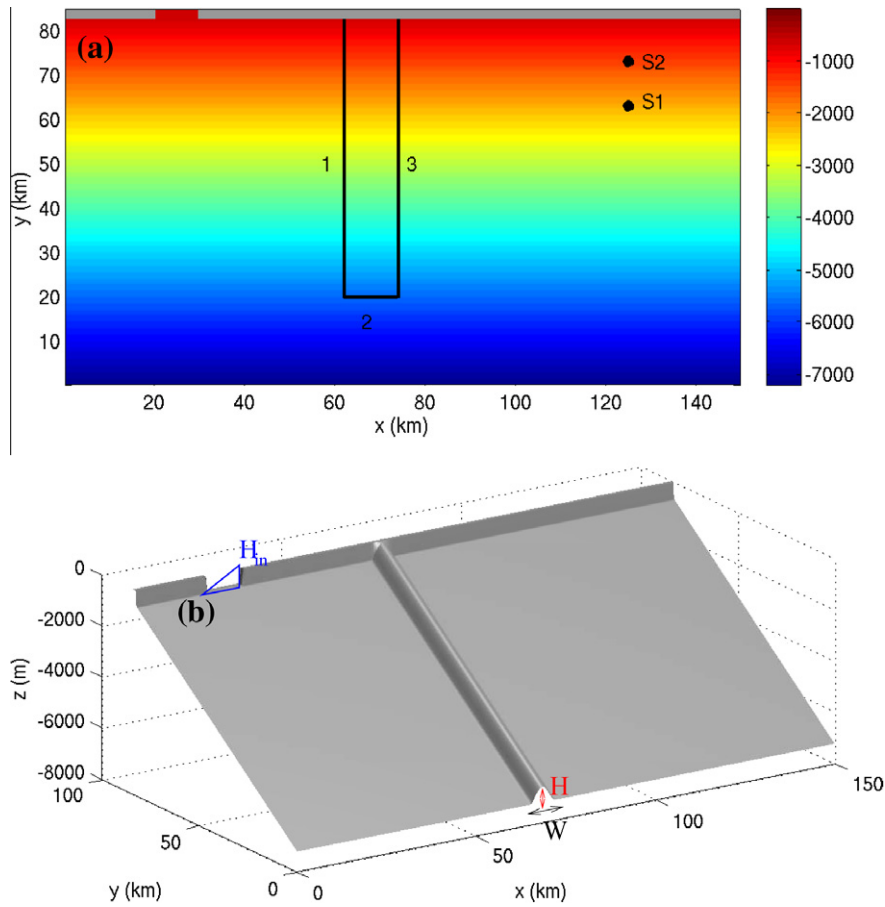


Fig. 1. (a) Plan view of the model geometry without a corrugation. Section locations to compute the entrainment are also shown as black lines. S1 and S2 are the station locations to compute the power spectra. (b) 3D view of the model geometry with $s = 0.08$ and a ridge.

idealized ocean is deep enough to minimize the reflection of the open boundary conditions at the southern side of the domain. A quadratic bottom drag formulation is used with a drag coefficient of $C_d = 2 \times 10^{-3}$ which is comparable to the overflow observations (Muench et al., 2009a). In this study, an f -plane approximation with the Coriolis parameter $f = -1.4 \times 10^{-4} \text{ s}^{-1}$ is employed. The characteristic method boundary conditions of Blayo and Debreu (2005) are applied to the east, west and south boundaries (see Appendix A for equations). In addition to open boundary conditions, a sponge layer is also used at $x > 140 \text{ km}$ to damp the density structure back toward the initial condition and remove the passive tracers that mark the overflow. The model is integrated for 40 days after the dense water is released from the north. This integration time is sufficient for the gravity current to reach the eastern boundary and achieve a quasi-steady state. The overflow reaches the boundary 10 days after the initial release, thus statistical data analysis are performed between 15 and 35 days. Surface stresses and buoyancy fluxes are set to zero everywhere in order to focus only on the variability of the flow due to corrugations.

Injection of the inflow in the channel is as follows. The dense overflow has its maximum thickness, H_m and velocity at the left-hand wall (when looking downstream) with a transport of

$$T_{in} = g' H_m^2 / (2f), \quad (3)$$

where $g' = g \frac{\Delta \rho}{\rho_0}$ is the reduced gravity. Initially, there is no stratification in the ambient water and the injected outflow is 0.2 kg m^{-3} denser than ambient water which leads to $g' = 0.0019 \text{ m s}^{-2}$. A parabolic profile is chosen for the inflow so that the minimum gradient

Richardson number ($Ri_g = -\frac{g}{\rho_0} \frac{\partial \rho}{\partial z} / (\frac{\partial u}{\partial z})^2$) is equal to 1/3 between the overflow and the ambient water. This condition minimizes the mixing in the channel and keeps the structure of the inflow constant. For further information about the inflow conditions, the reader is referred to Legg et al. (2006).

Table 1

Experimental setup for ridges and canyons with different height, H , and width, W using $s = 0.08$, $f = -1.4 \times 10^{-3} \text{ s}^{-1}$, $g' = 1.9 \times 10^{-3} \text{ m/s}^2$ and $H_m = 150 \text{ m}$.

Exp	Height [m]	Width [m]	Aspect ratio (H/W)
1	50	2000	0.025
2	150	2000	0.075
3	300	2000	0.15
4	600	2000	0.3
5	800	2000	0.4
6	1000	2000	0.5
7	1200	2000	0.6
8	50	4000	0.0125
9	150	4000	0.0375
10	300	4000	0.075
11	600	4000	0.15
12	800	4000	0.2
13	1000	4000	0.25
14	1200	4000	0.3
15	50	6000	0.00833
16	150	6000	0.025
17	300	6000	0.05
18	600	6000	0.1
19	800	6000	0.1333
20	1000	6000	0.1666
21	1200	6000	0.2

A reference experiment with no topographic corrugation serves as a control case. A total of 42 perturbation experiments are conducted with 7 different heights, H , and 3 widths, W (Table 1), for a ridge and a canyon (21 simulations each). This set of experiments provides information about the modification of transport, along-slope location and entrainment of the overflow due to corrugations with different aspect ratios. Fourteen additional experiments are performed with different Coriolis accelerations, f , different reduced gravities, g' , and different initial thicknesses of the inflow, H_{in} . These latter experiments help us understand the effect of ridges when the upstream properties of the overflow change.

3. Results

3.1. The initial propagation of the modeled overflow

A passive dye is injected with the overflow in the channel. A plan view of the vertically integrated passive tracer concentration for the reference case (i.e. no corrugation) is shown in Fig. 2. After the overflow is released, the gravity current flows downslope and to the left due to the Earth's rotation (recall $f < 0$). The dense overflow never reaches its neutral buoyancy since there is no ambient stratification. However, the overflow becomes geostrophically adjusted and follows the isobaths (Fig. 2(b)). Cenedese et al. (2004) described three regimes for a dense current flowing down a sloping topography depending on the Froude, Fr , and the Ekman, Ek , numbers. The first regime is laminar flow which was observed for $Fr < 1$. The second regime is the so-called roll-wave regime which was observed for $Fr \geq 1$ and $0.05 < Ek < 5$. The last regime is the eddy regime which occurs for $Fr < 1$ and $0.01 < Ek < 0.1$. In our control run, $Fr = u/\sqrt{g'H_{in}} \approx 0.6$ and the Ekman number is $Ek = (\delta_E/H_{in})^2 \approx 0.01$ where $\delta_E = C_d g' \alpha / f^2$ is the bottom Ekman depth and $\alpha \approx \sqrt{s^2 + (H/W)^2}$ (Wahlin, 2002) where s is the background

slope. Three distinctive cyclones in Fig. 2(c) indicate that the flow is indeed in the eddy regime. After 10 days, the overflow follows the topography and reaches the eastern boundary (Fig. 2(d)). Previous studies (Spall and Price, 1998; Ezer, 2006; Ilıcak et al., 2011) also show cyclogenesis in overflow systems. Spall and Price (1998) argue that the potential vorticity (PV) conservation might be responsible to generate cyclonic vortices. The exact mechanism to generate eddies in the gravity currents is beyond the scope of this paper.

Next, we look at the frequencies of the eddies formed by the overflow. Two different stations, S1 and S2, are selected away from the inflow area (see Fig. 1(a) for location of the stations). Fig. 3(a) and Fig. 3(c) display the time series of tracer concentration at station S1, 50 meter above bottom (mab) and S2, 70 (mab) respectively. There is strong temporal variability not only in tracer but also in velocities (not shown). Power spectra are computed for both time series. Fig. 3(b) and Fig. 3(d) clearly indicate three distinct signals in the overflow; (i) 14 h, 30 h and 60 h of oscillations for the station S1, (ii) 13 h, 30 h and 75 h of oscillations for the station S2. These three signals can be seen at all depths (not shown), thus the oscillations are close to barotropic. Darelius et al. (2009) describe that the Filchner overflow also has three different oscillations; 35 h, 70 h and 140 h in addition to the tides. They observe that oscillations in temperature are accompanied by oscillations in velocity and they are both barotropic. They propose three possible mechanisms for these temporal variabilities: (i) eddies generated by vortex stretching (ii) eddies generated by baroclinic instabilities and (iii) continental shelf waves due to atmospheric forcing. However, Wilchinsky and Feltham (2009) argue that the variability is not related to the continental shelf waves since the variability is observed for both the temperature and the velocity. The latter should be oscillated if the shelf waves were responsible for the fluctuations.

However, our control run is not intended to simulate the Filchner overflow exactly since the latter encounters two ridges after it

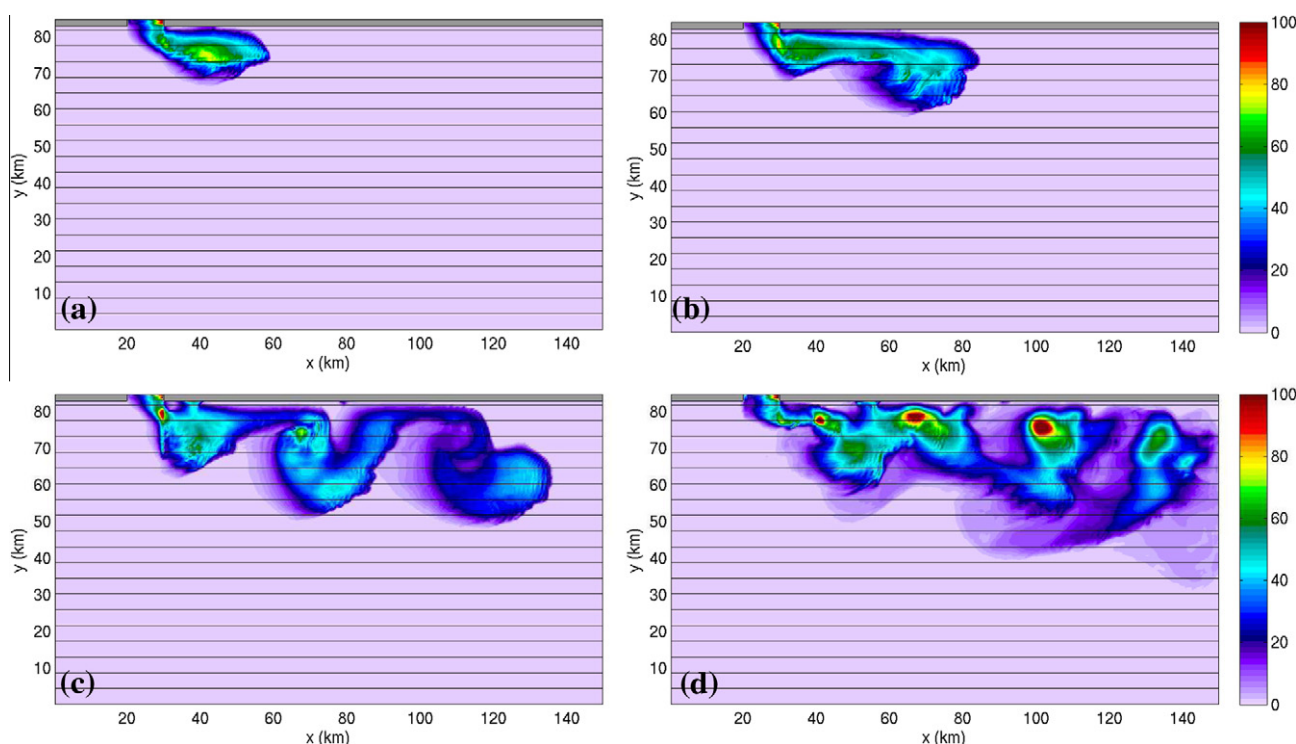


Fig. 2. Plan view of the vertically integrated passive tracer concentration for the control run at a time (a) 1.25, (b) 2.5, (c) 5, (d) 10 days. Depth contours are shown in black lines.

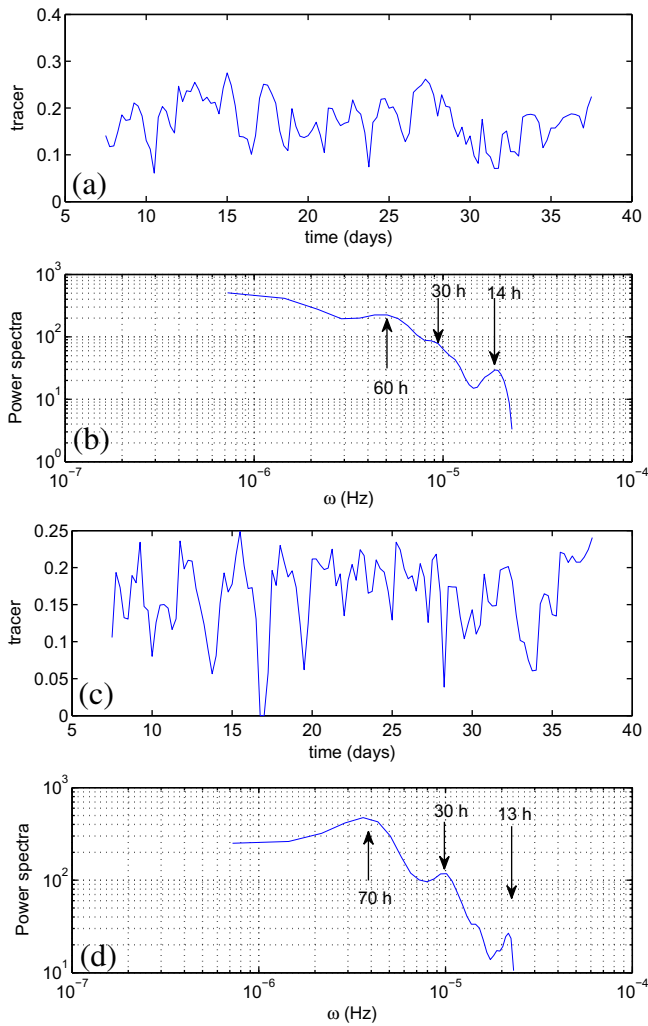


Fig. 3. (a) Tracer concentration in time at station S1 and 50 meter above bottom (mab) for the control case. (b) Power spectra of tracer vs. frequency for the control case at station S1. (c) Tracer concentration in time at station S2 and 70 meter above bottom (mab) for the control case. (d) Power spectra of tracer vs. frequency for the control case at station S2.

flows out from the continental shelf. To this end, we performed an additional experiment with an idealized bathymetry of the Weddell Sea. Two ridges are included in the model topography; both of them have a cosine shape with a width of 8 km. The first ridge (on the left) has a maximum height of 300 m and starts from 1500 m depth until 3500 m depth (Fig. 4(a)). The second ridge (on the right) has maximum height of 500 m and starts from about 800 m depth until 2500 m depth (Wang et al., 2009). The model is integrated 120 days. Fig. 4(a) displays the vertically averaged tracer field at time = 60 days. It is clear that both ridges steer the flow downslope. Two cyclones are visible around $x \approx 230$ km and $x \approx 270$ km. We choose two stations before and two stations after the ridges. The station locations are similar to those in Darelius et al. (2009). Tracer fields at 100 mab and 50 mab for stations S3, S4, S5 and S6 are shown in Fig. 4(b) and (c), respectively. Power spectra of the tracer fields show similar magnitude oscillations as seen in the control run (Fig. 4(d) and (e)). The same order of magnitude of variability is also seen in our simulation without any atmospheric forcing. Therefore, we believe that the observed fluctuations are due to the eddies generated by the vortex stretching described above. This result is also consistent with the one described by Wang et al. (2009).

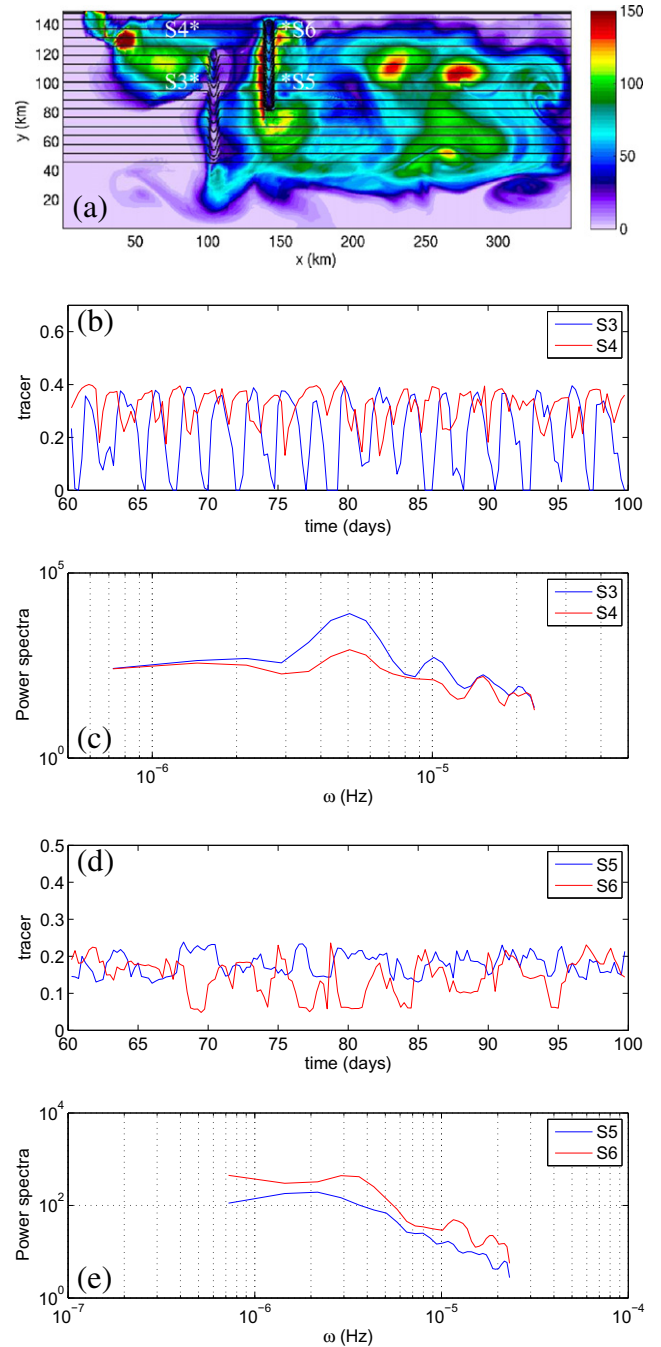


Fig. 4. (a) Plan view of the vertically integrated passive tracer concentration at time = 60 days. S3, S4, S5 and S6 are the station locations to compute the power spectra. (b) Tracer concentration in time at station S3 (100 mab) and S4 (100 mab). (c) Power spectra of tracer vs. frequency at station S3 and S4. (d) Tracer concentration in time at station S5 (50 mab) and S6 (50 mab). (e) Power spectra of tracer vs. frequency at station S5 and S6.

3.2. The steering of the overflow by ridges and canyons

In this section, ridges and canyons with different aspect ratios are investigated. Figs. 5 and 6 display vertically integrated tracer concentration for different ridges and canyons, respectively. The tracer weighted overflow thickness for the control run is shown in Figs. 5(a) and 6a at time = 20 days. Fig. 5(b) displays the domain with a ridge which has a height of 150 m and a width of 6 km ($H_{in} = 150$ m). Since the aspect ratio of the ridge is small, the flow seems only slightly affected. There are still two eddies visible in

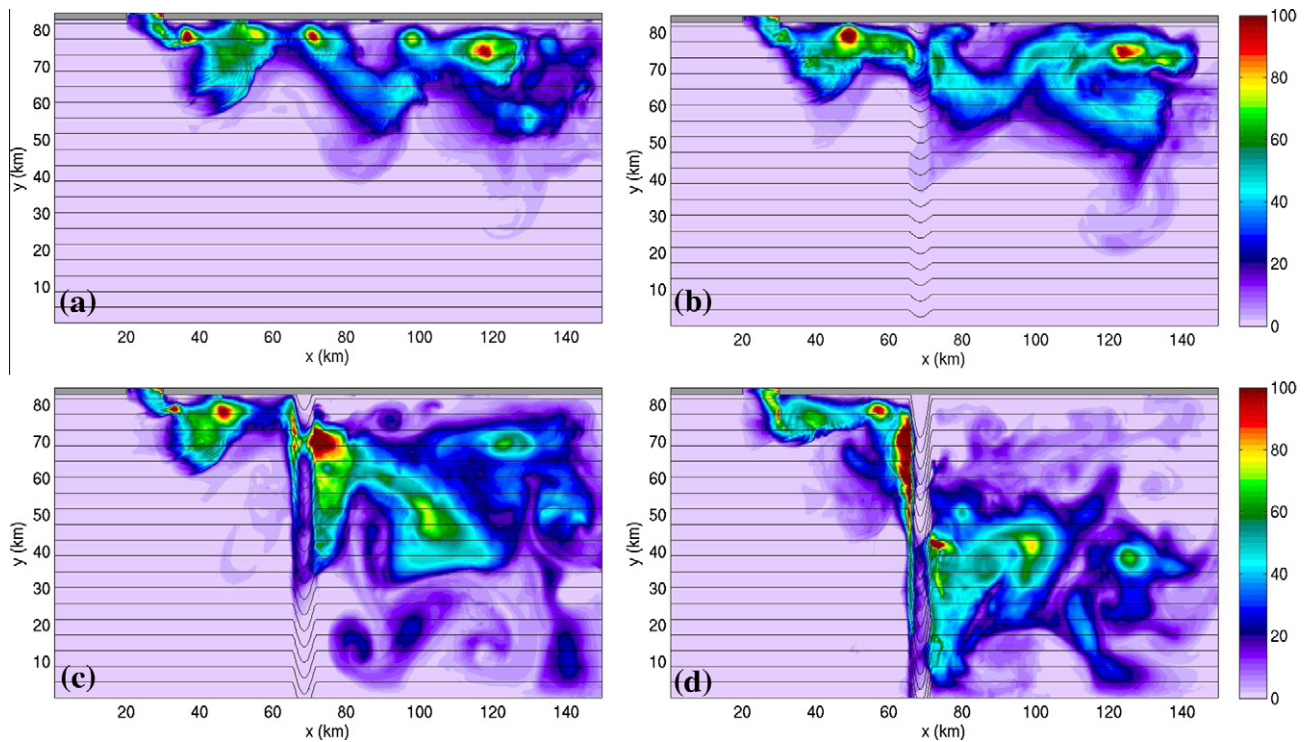


Fig. 5. Plan view of the vertically integrated passive tracer concentration at a time 20 days after the release of the dense overflow for different cases: (a) control run ($H = 0$), (b) ridge $H = 150$ m; $W = 6$ km, (c) ridge $H = 600$ m; $W = 6$ km, (d) ridge $H = 1200$ m; $W = 6$ km. Depth contours are shown in black lines.

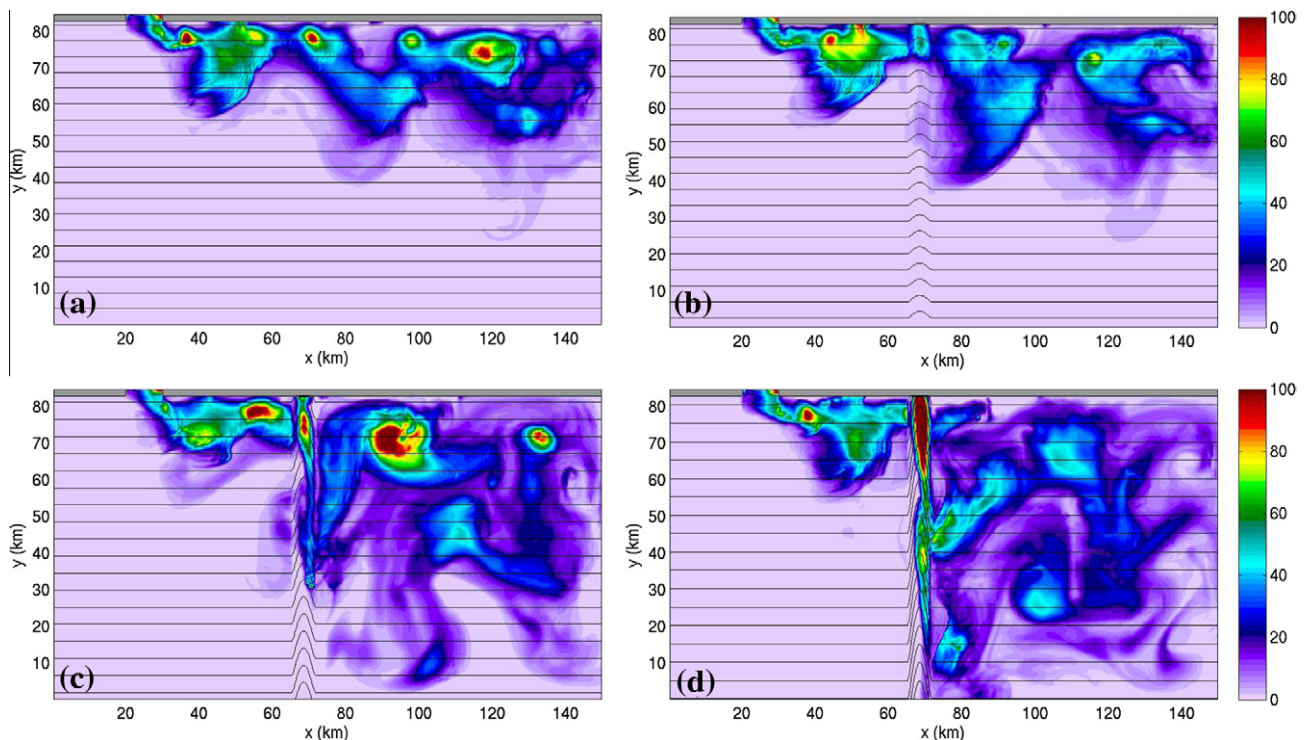


Fig. 6. Same as Fig. 5 but for canyons.

the domain. However, when the height of the ridge is increased up to 600 m, the flow is changed dramatically (Fig. 5(c)). When the plume reaches the corrugation, the flow is steered downslope by the ridge. The dense water becomes much wider when it passes to the other side of the corrugation. The gravity current is trans-

ported to the deeper ocean due to the existence of the ridge. The tracer concentration can be found as far as $y = 30$ km south at the upstream side of the corrugation. The vertically integrated thickness of the overflow at the downstream side of the ridge is up to 100 m. This indicates that the overflow entrains ambient fluid

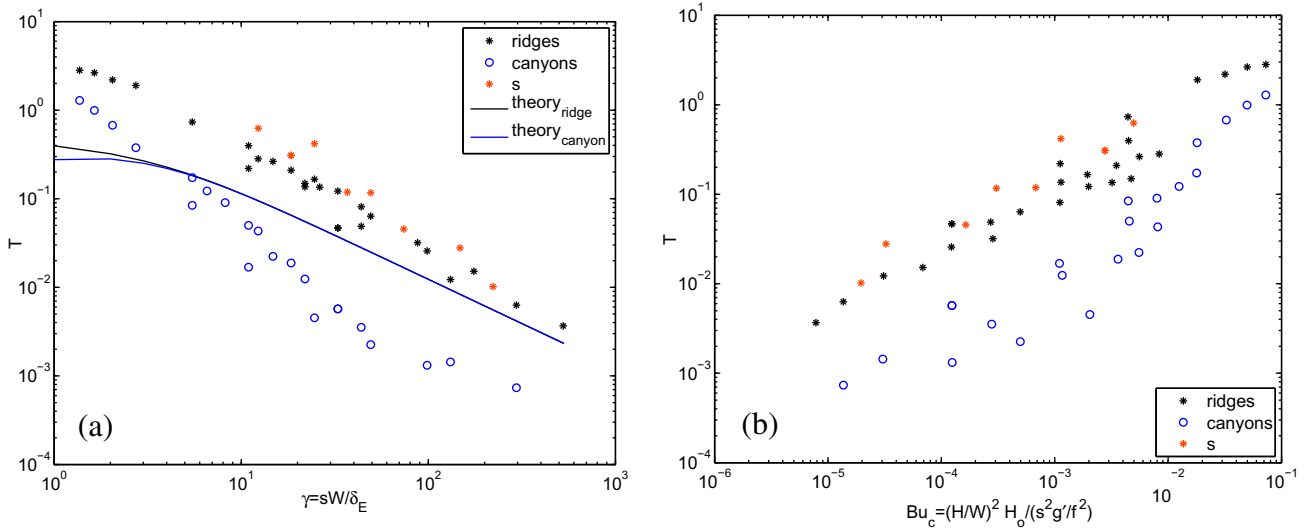


Fig. 7. (a) Non-dimensional transport of corrugations vs. γ . (b) Non-dimensional transport of corrugations vs. Bu_c .

when it passes over the ridge. The overflow is even transported to 9000 m depth and reaches the southern boundary at the end of the domain. When the height of the ridge is increased to 1200 m, the overflow is piled up and transported to the deep ocean predominantly on the upstream side of the ridge (Fig. 5(d)). Most of the overflow is deeper than $y = 40$ km at the downstream side of the corrugation. This means that the mean path of the overflow is shifted off-shore.

The dynamics of the overflow passing over a canyon are similar to the dynamics of the gravity current in the ridge case. Fig. 6(b) displays the overflow passing a canyon which has a depth of 150 m and a width of 6 km. Once again, the overflow is not affected by the corrugation with a small aspect ratio. The steering of the flow by a canyon is more visible when the depth of the canyon increased to 600 m (Fig. 6(c)). The plume becomes much wider and spreads to the deeper part of the ocean. Fig. 6(d) displays the canyon with $H = 1200$ m and $W = 6$ km. The qualitative pictures are similar in the ridge and the canyon cases; the overflow is steered downslope and some overflow fluid crosses over the corrugation to the other side. The steering and mixing increase with higher topographic aspect ratios in the gravity current flowing over the corrugation.

The analytical theory developed by Wahlin (2002) predicts the non-dimensional transport capacity for a given corrugation shape. The theory predicts that corrugations have maximum transports depending on a nondimensional parameter $\gamma = sW/\delta_E$, where s is the background slope, W is the width of the corrugations and δ_E is the bottom Ekman depth (Wahlin, 2002; Darelius and Wahlin, 2007; Darelius, 2008). When the overflow transport, T_o , is less than the maximum transport of the corrugation, T_c (where T_c is a function of γ , see Eqs. (21) and (24)), the theory predicts that no dense water should cross over the corrugation. However, the theory is developed for a steady state solution so that the flow has to be stationary for the dense water to remain in a canyon. Steady state implies that the net transport across the corrugation must be zero, which can be satisfied only if the Ekman transport in the canyon is balanced by the geostrophic component (Wahlin, 2002). On the other hand, in all our simulations the dense plume passes over the corrugation even with large aspect ratios (i.e. smaller γ). One possible explanation might be that the eddies break the balance between geostrophic and Ekman transport, and that the eddies can carry the water past on the side of the ridges even when $T_o < T_c$. In addition to this, the analytical theory assumes that mixing is

negligible and the Burger number, $Bu = g'H/(f^2W^2)$, is small. In our idealized experiments Bu is comparable to or larger than unity, and there is strong mixing which will increase the overflow transport and the height of the overflow while reducing g' .

Darelius and Wahlin (2007) find that the maximum transport of the corrugation for a given γ is larger for ridges than for canyons, since the walls of a canyon limit the lateral extent of the dense flow and the transport of the corrugation has to increase when γ decreases. The entrainment is often a function of Richardson number which can be defined

$$Ri = \frac{-\frac{g}{\rho_0} \frac{\partial \rho}{\partial z}}{\left(\frac{\partial u}{\partial z}\right)^2} \approx \frac{-\frac{g}{\rho_0} \frac{\Delta \rho}{H_o}}{\left(\frac{U}{H_o}\right)^2} = \frac{g'H_o}{U^2} = \frac{1}{Fr^2}, \quad (4)$$

where Fr is the Froude number and H_o is the overflow thickness upstream of the corrugation. The geostrophic velocity (U) can be scaled with the Nof speed $U \sim g's/f$ (Nof, 1983). This would give an estimate of the Froude number: $Fr = \sqrt{\frac{g's}{H_o f}}$. To compare with

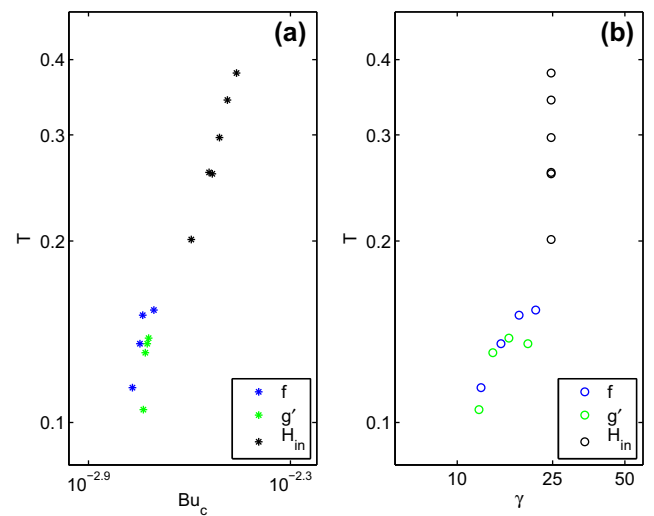


Fig. 8. (a) Non-dimensional transport of the ridge ($H = 600$ m and $W = 6$ km) changing f , g' and H_{in} vs. Bu_c . (b) Non-dimensional transport of the ridge ($H = 600$ m and $W = 6$ km) changing f , g' and H_{in} vs. γ .

theory, we examine the maximum transport of ridges and canyons with respect to two non-dimensional numbers: γ and a corrugation Burger number defined as

$$Bu_c = \frac{1}{Fr^2} \left(\frac{H}{W} \right)^2 = \frac{H^2}{W^2} \frac{1}{s^2} \frac{H_0}{g'/f^2}. \quad (5)$$

Note that the corrugation Burger number, Bu_c , is different than the original Bu . The former is a function of Richardson number and aspect ratio of the corrugation. We find that Bu_c is more suitable to describe and parameterize the flow (as discussed in Section 3.4). Fig. 7(a) and (b) show the non-dimensional maximum transport of the corrugations for different γ and Bu_c , respectively. The transport of a corrugation is normalized by $\hat{T} = \frac{g'}{f} (sW)^2$ as described in

(Davies et al., 2006). In the experiments shown in Figs. 7(a) and 6(b), γ and Bu_c are changed by changing either height (H) or width (W) of the canyon (see Table 1). In the ridge case, an additional eight experiments are performed changing the background slope ($s = 0.04, 0.06$) with a width of 6 km and different heights of $H = 50, 150, 300, 600$ m, respectively (red stars in Fig. 7(a) and (b)). It can be clearly seen that ridge transports (black stars) are larger than canyon transports (blue circles) at the same γ as expected by the theory. There is a clear correlation between the transport, T , and γ and Bu_c . When H of a ridge increases (holding W constant), the non-dimensional parameter γ , which can also be defined as

$$\gamma = \frac{sW}{C_d \frac{g'}{f^2} \sqrt{s^2 + (H/W)^2}} \quad (6)$$

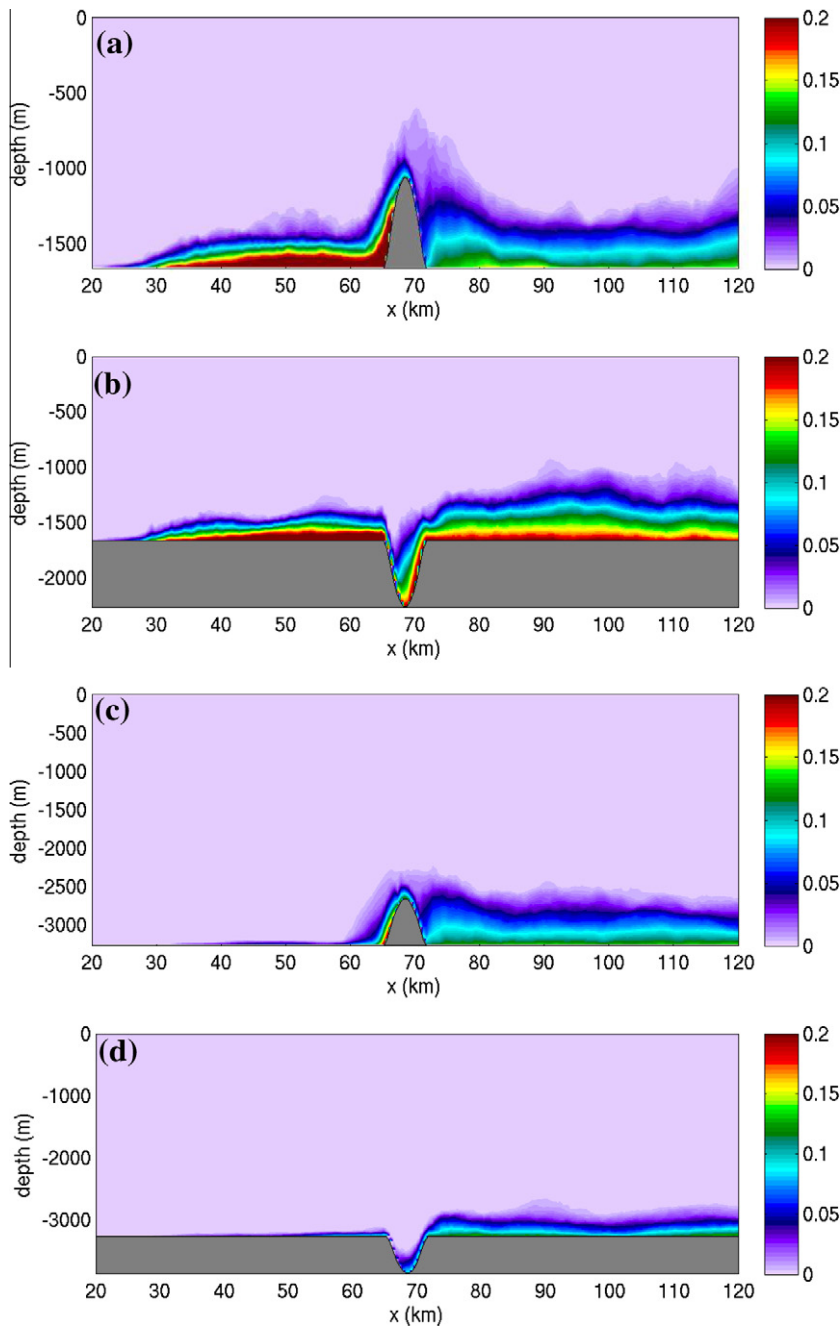


Fig. 9. Vertical section of averaged tracer at $y = 70$ km for (a) ridge with $H = 600$ m and $W = 6$ km (b) canyon with $H = 600$ m and $W = 6$ km. Averaged tracer values are computed in geopotential coordinates. Vertical section of averaged tracer at $y = 50$ km for (c) ridge with $H = 600$ m and $W = 6$ km (d) canyon with $H = 600$ m and $W = 6$ km. Averaged tracer values are computed in geopotential coordinates.

decreases and Bu_c increases. This means that the ridge can steer more dense water into the deep ocean, thus the cross-slope transport of the ridge increases. On the other hand, if H is kept constant and W increases, γ increases and Bu_c decreases. In this case, the maximum transport goes down since the slope of the corrugation becomes more gentle (i.e. H/W decreases) and the ridge or canyon carries less dense water to the deep. The theoretical values of a cosine shaped ridge and canyon (see Appendix B for solutions) are also computed (black and blue lines in Fig. 7(a)). Darelus (2008) finds that the theory overestimates the transport of the corrugations in the laboratory experiments. We can see that canyon transports are below the theoretical values. However, the transports of the ridges are above the theoretical values, which indicates that the simulated flow carries more than the analytical estimation.

We also perform fourteen additional experiments with a fixed ridge geometry (with $H = 600$ m and $W = 6$ km) changing the Coriolis parameter ($f = -1, -1.1, -1.2, -1.3 \times 10^{-4} \text{ s}^{-1}$), reduced gravity ($g' = 0.0024, 0.0029, 0.0033, 0.0038 \text{ ms}^{-2}$) and initial overflow thickness ($H_{in} = 200, 250, 300, 350, 400, 450$ m), respectively. The maximum transport that the ridge carries for these new experiments is shown in Fig. 8. Changing f (blue points) and g' (green points) do not effect the non-dimensional transport significantly since the transport is normalized by $\hat{T} = \frac{g'}{f^2} (sW)^2$. On the other hand, when the initial overflow thickness increases, the cross-slope transport of the ridge also increases (black points in Fig. 8(a)). On the other hand, increases in transport due to increases in H_{in} can not be represented using γ (black circles in Fig. 8(b)). Thus, we focus on the dependence of properties on Bu_c since it contains information on the corrugation, H^2/W^2 , and information on the upstream properties of the overflow, $H_o/(s^2g'/f^2)$.

Time-averaged vertical sections of tracer for a ridge and a canyon with $H = 600$ m and $W = 6$ km are shown in Fig. 9. The dense overflow piles up on the upstream side of the ridge. The flow is thinnest at the top of the ridge, then the thickness of the overflow increases rapidly at the end of the corrugation (Fig. 9(a)). Deformations of the density field at $x \approx 73$ km clearly indicate a presence of a hydraulic jump. There is strong mixing after the edge of the corrugation since the tracer is diluted and the densest layer (shown in red) disappears on the right side of the ridge. In the canyon case, the overflow leans on the right side of the corrugation (looking northward in Fig. 9(b)). Once again, there is a small jump in the density field at $x \approx 73$ km. On the right side of the canyon, there is still fluid in the densest (red) layer which indicates less mixing with respect to the ridge case (to be discussed in Section 3.3).

The effect of corrugations can also be seen in the mean off-shore distance of the overflow plume. We compute the mean position of the overflow as a function of along slope distance for different corrugation cases:

$$\bar{Y}_\tau = \frac{\int y\tau(x,y,z)dydz}{\int \tau(x,y,z)dydz}, \quad (7)$$

where τ is the passive tracer. We only consider τ where it is greater than 0.05. The mean plume locations in y -direction for different heights of ridges are shown in Fig. 10(a). The control run plume travels along isobaths 15 km downslope from the source (green line). A small vertical ridge with a height of 50 m or 150 m does not change the direction of the flow significantly and the mean plume path is slightly below the control run plume path (black and blue lines). However, when the height of the ridge is increased to 300 m, the flow is steered downslope and travels along $y = -20$ km down from the source (red line). It can be clearly seen when the height of the ridge increases, the flow travels to the deeper part of the ocean (i.e. downslope in the y -direction). This is consistent with the maximum transport of the corrugation analysis. Increasing H leads to increased Bu_c , thus the ridge steers the overflow water fur-

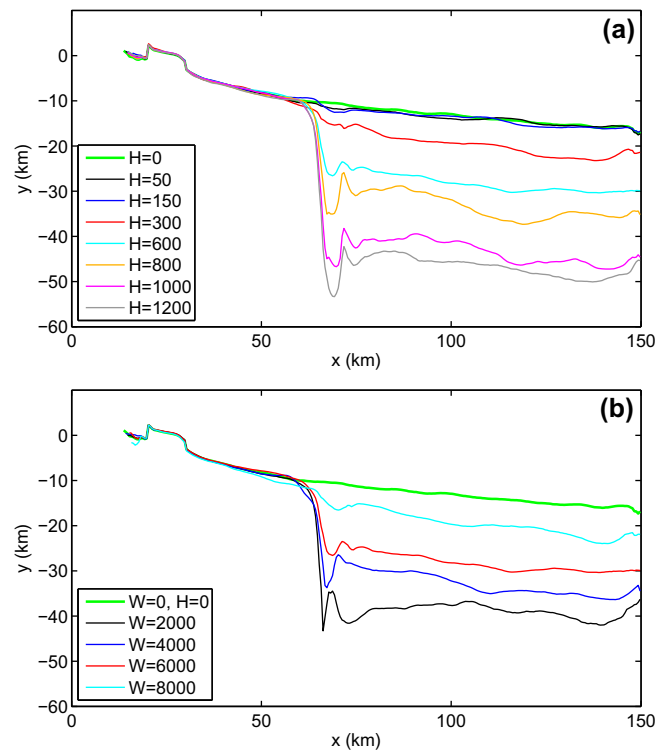


Fig. 10. (a) The tracer-weighted overflow path for ridges with different heights but constant width ($W = 6$ km). (b) The tracer-weighted overflow path for ridges with different widths but constant height ($H = 600$ m). Note that y – axis is away from the northern wall.

ther downslope. Fig. 10(b) displays the tracer-weighted overflow path for ridges of different widths. The heights of these ridges are kept constant at $H = 600$ m. For the 8 km wide ridge, the plume path is at approximately 20 km down (cyan line) from the inflow channel since the slope of the ridge is gentler compared to the other ridges with the same height. When the width of the ridge decreases, Bu_c increases which leads to more downslope transport and a path lower down the slope (Fig. 10(b)).

To summarize, corrugations such as ridges and/or canyons may steer the plume downslope. The analytic theory developed by Wahlin (2002) and Darelus and Wahlin (2007) suggests that the flow is governed by a single parameter γ (Eq. (6)). However, we find that the corrugation Burger number, Bu_c (Eq. (5)), is a better parameter to describe the flow over topography since it includes the dependence on overflow thickness. Our idealized simulations show that ridges are more effective than canyons in transporting the overflow to the deeper ocean as predicted by the theory. The main reason behind this is that the flow in the canyon is limited by the canyon walls. The maximum downslope transport of a corrugation can be increased when the height of the corrugation increases (i.e. γ decreases or Bu_c increases) or when the width of the corrugation decreases (i.e. γ increases or Bu_c decreases).

3.3. Transport and mixing

The overflow thickness and alongslope transport are good indicators for the mixing in gravity current simulations (Legg et al., 2006; Ilıcak et al., 2008a). Tracer weighted overflow thickness, h_o is defined as

$$h_o(x) = \frac{\int h(x,y,z)\tau(x,y,z)dydz}{\int \tau(x,y,z)dydz}, \quad (8)$$

where h is the height above the bottom. Fig. 11(a) displays the mean overflow thickness as a function of along-slope distance for ridges

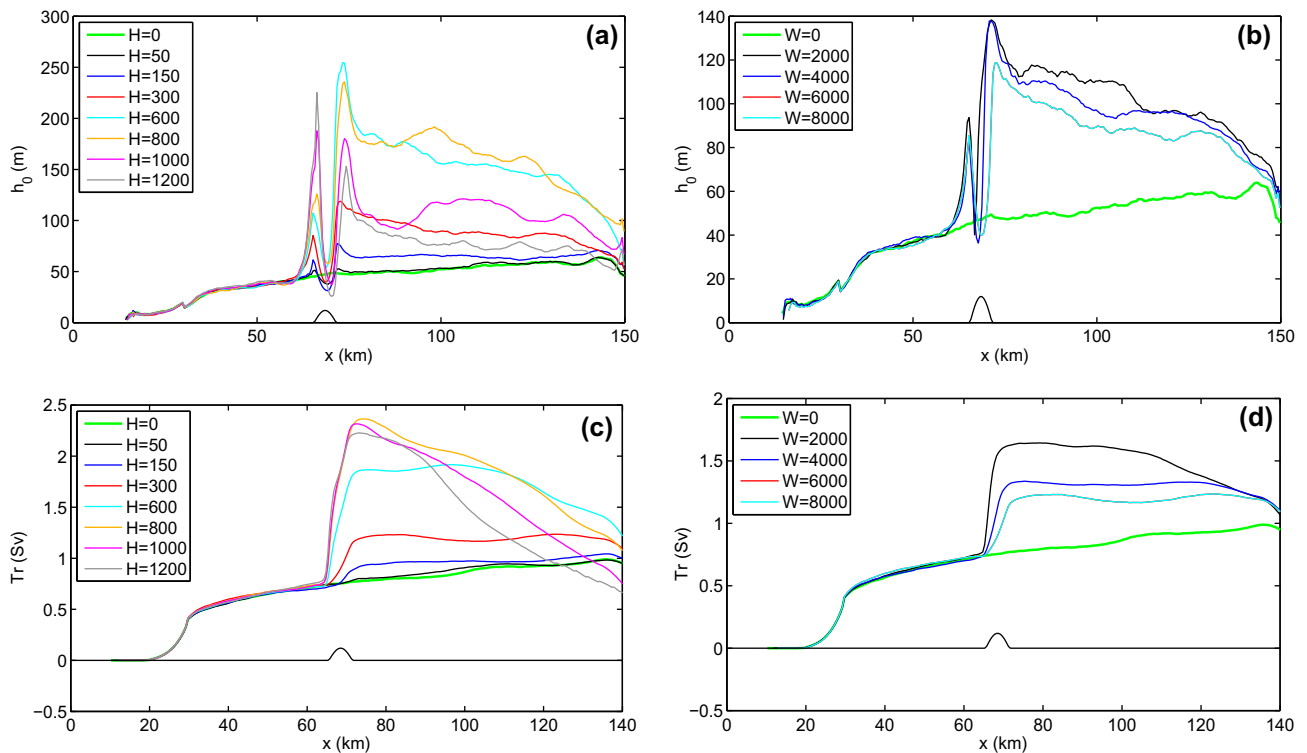


Fig. 11. (a) Tracer weighted overflow thicknesses for ridges with different heights but constant width ($W = 6$ km). (b) Tracer weighted overflow thicknesses for ridges with different widths but constant height ($H = 300$ m). (c) The eastward transport of water with $\tau > 0.05$ in the overflow for ridges with different heights but constant width ($W = 6$ km). (d) The eastward transport of water with $\tau > 0.05$ in the overflow for different widths but constant height ($H = 300$ m). Ridge locations are shown with black lines.

with different heights but constant width ($W = 6$ km). A steady increase in the overflow thickness can be seen in the control case (green line) because of the entrainment of ambient water. The tracer weighted overflow thickness is around 60 m for the control case when the flow reaches the boundary. The outflow thicknesses in all the ridge simulations are similar to the control run until $x = 60$ km. After that, the overflow encounters the ridge and piles up (h_o increases) and then drops suddenly (h_o decreases at around $x = 69$ km at the top of the crest). The second increase in h_o is due to the hydraulic jump just after the corrugation. The statistically steady overflow thicknesses are consistent with the vertical sections described in the previous section. In all the ridge simulations, the overflow thickness after the corrugation is larger than the one in the control run due to the mixing that occurs at the ridge area. It seems that the maximum overflow thickness ($h_o \approx 160$ m) occurs for the ridge with a height of 800 m (yellow line in Fig. 11(a)). The overflow thickness starts to decrease after $x = 140$ km since this is the beginning of the sponge area. The overflow thicknesses for a constant $H = 300$ m and different widths are shown in Fig. 11(b). The slope of a ridge (H/W) increases when the width of the ridge decreases. This leads to an increase in h_o since stronger mixing occurs in sharper corrugations. The ridge with a larger slope ($W = 2$ km, $H/W = 0.15$, black line in Fig. 11(b)) has a thickness of 100 m. On the other hand, the ridge with a gentle slope ($W = 8$ km, $H/W = 0.0375$, cyan line in Fig. 11(b)) only has a thickness of 80 m.

Next, we compute the overflow transport in the along-shore direction as

$$Tr(x) = \int_A U dy dz, \quad (9)$$

where A is the region where $\tau > 0.05$ and U is the zonal mean velocity. Fig. 11(c) displays the eastward transport for the simulations with a constant width and different heights. The total transport in the control run increases until the end of the domain (green line).

In all the ridge simulations, the transport suddenly increases when the overflow meets the corrugation and the transport is always larger than the one in the control run after the corrugation. The maximum transport occurs at the ridge with the height of 800 m, consistent with the maximum overflow thickness in Fig. 11(a). Note that the decrease in the transport for the ridges with 1000 m and 1200 m heights after $x \approx 90$ km indicates that either the flow has not reached steady-state for these cases or the water is becoming so dilute that $\tau < 0.05$ over much of the plume. The overflow thickness and transport analysis indicate that the mixing increases with increasing height of the ridge.

Finally, we look at the entrainment rate of the overflow due to the corrugation. An entrainment coefficient can be defined as diapycnal velocity, w_E , divided by the mean or characteristic velocity (Riemenschneider and Legg, 2007). In this study, we employ bulk computation using the transports to compute the entrainment coefficient;

$$E = \frac{w_E}{\bar{U}^t} = \frac{(\bar{Tr}_3^t + \bar{Tr}_2^t) - \bar{Tr}_1^t}{\bar{U}^t S^t}, \quad (10)$$

where w_E is the bulk diapycnal velocity, T_1 , T_2 and T_3 are the transports of $\tau > 0.05$ water through Sections 1–3 (for section locations see Fig. 1(a)). \bar{U} is the mean velocity computed at the upstream of the corrugation and S is the surface area of the $\tau > 0.05$ surface in the region bounded by the sections. All quantities are time averaged between 15 and 35 days after the flow has reached a quasi steady-state.

Fig. 12 shows the normalized entrainment coefficient for different ridge scenarios. The control case entrainment coefficient (E_0) is employed to normalize E . Note that, since the initial transport depends on g' , f and H_{in} (Eq. (3)), a new control run has to be run when we change those variables. There is a strong correlation between Bu_c and E/E_0 . For the ridge with $W = 6000$ m, E/E_0 is the

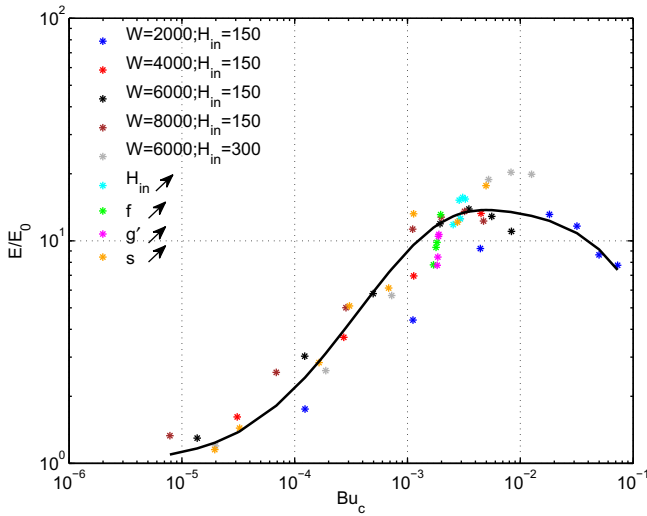


Fig. 12. Normalized entrainment vs. Bu_c for different cases.

smallest for $H = 50$ m since the overflow can easily pass over the ridge. The mixing is the largest when the $H = 800$ m (black stars in Fig. 12). The entrainment increases when the height of the corrugation increases (larger Bu_c) until a threshold point, after which the entrainment starts to decrease. The reason behind this decrease is that the flow is directed downslope instead of crossing over the ridge, so that it entrains less when $H \geq 1000$ m. This is consistent with the analysis of the overflow thicknesses (Fig. 11(a)) where h_0 increases up to 200 m for the $H = 800$ m ridge, then h_0 drops for higher ridges. The normalized entrainment values do not change significantly when we change g' and f (magenta and green stars in Fig. 12). When initial thickness, H_{in} , is increased in the model, the entrainment also increases since h_0 increases.

3.4. Parameterization

In order to derive a function able to account for the under representation of mixing due to unresolved corrugations in future coarse simulations, we fit empirically the dependency of the averaged normalized entrainment coefficient on the corrugation Burger number. To derive a generic function, there are two boundary conditions to be satisfied; a) in the case of no corrugation ($Bu_c = 0$), the function has to be unity since E has to be equal to E_0 , b) in the case of a vertical wall that goes all the way to the surface (i.e. $Bu \rightarrow \infty$), the function has to go to zero. To this end, the following exponential function is proposed

$$\frac{E}{E_0} = f(Bu_c) = a \times e^{(-b \times Bu_c)} + c \times e^{(-d \times Bu_c)}, \quad (11)$$

where the best-fit coefficients are

$$a = 14.55 \quad b = 9.2961 \quad c = -13.55 \quad d = 914.7. \quad (12)$$

We also try different functions (polynomial, sin, etc.), however the exponential function is the best fit. The first boundary condition is ensured by $a + c = 1$ and the second boundary condition is satisfied since the exponential terms are bounded. In Fig. 12, the black curve is obtained using Eq. (11) for different corrugation Burger numbers.

To implement the new function, first we have to revisit how the model handles the mixing. Since GOLD is an isopycnic model, the eddy diffusivity has to be converted to the diapycnal velocity which is proportional to the entrainment. Thus, we can assume that κ in the resolved corrugation cases can be also proportional to the κ in the control case,

$$\frac{\kappa_{corrugation}}{\kappa_0} \sim \frac{E}{E_0} = f(Bu_c). \quad (13)$$

We propose a new parameterization which is a modified version of Eq. (1),

$$\frac{\partial^2 \kappa}{\partial z^2} - \frac{\kappa}{L_d^2} = -2\tilde{S}F(\tilde{Ri}), \quad (14)$$

where $\tilde{S} = Sf(Bu_c)$ is a modified vertical shear enhancing the resolved shear S by a factor $f(Bu_c)$ to account for the unresolved shear in a coarse resolution model. In addition to Eq. (14), the modified vertical shear is also used to compute the gradient Richardson number and the turbulent kinetic energy, thus $\tilde{Ri} = N^2/\tilde{S}^2$ is decreased while κ is increased locally around the corrugation area. These changes will lead to additional mixing in the model.

To investigate the performance of the new parameterization, three experiments using Eq. (14) are performed with a coarse resolution model (without corrugations). Since we do not want to change the upstream conditions, horizontal resolution is kept constant ($\Delta x = 500$ m) until $x = 50$ km and starts to increase up to $\Delta x = 8$ km using a hyperbolic function. Three different experiments are employed to try to reproduce a ridge with a 6 km width and a height of $H = 150$, $H = 300$ and $H = 600$ m, respectively. Fig. 13(a) displays the vertically integrated tracer for the experiment that simulates the ridge with $H = 600$ m. In the high resolution case, the ridge was located $65.5 \leq x \leq 71.5$ km. The new parameterization increases mixing around the same location. The flow becomes laminar after $x = 50$ km because of the coarse resolution. Since the new parameterization effects only the vertical shear, there is no downslope transport unlike the high resolution case. Fig. 13(b) shows time and meridional average of the overflow thickness for the cases with the new parameterization (i.e. no corrugation) and

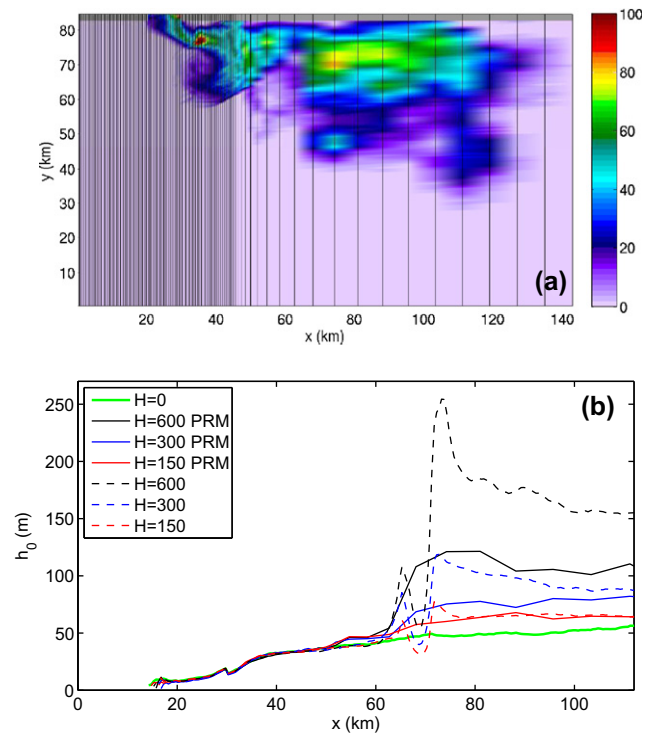


Fig. 13. (a) Plan view of the vertically integrated passive tracer concentration at a time 20 days for the model without 600 m ridge but with the new parameterization. Horizontal grid locations are shown in black lines. (b) Along-slope distance vs. tracer weighted overflow thicknesses with the ridges explicitly resolved in the high resolution models (dashed lines) and with the new parameterization (PRM) in coarse resolution models (solid lines).

without the parameterization (i.e. resolved corrugation). The sudden increase of the thicknesses in the unresolved ridge cases is clearly seen (solid lines). There is a reasonable agreement in the $H = 150$ m and $H = 300$ m ridge cases (red and blue lines). However, for the $H = 600$ m ridge, the overflow thickness is around 160 m with a resolved corrugation and only 110 m with the parameterization. The overflow transports with the new parameterization are also in agreement with those in the high resolution cases (not shown).

4. Discussion and conclusion

Dense and intermediate water masses are crucial for the global meridional overturning circulation. Many of these waters must flow over ocean canyons/ridges or down continental slopes. The mixing around these topographic features is an important process determining the final properties and quantity of the overflows.

In this study, we attempt to understand the dynamics of the overflow as it passes over a single corrugation. The main goal is to improve our understanding of the interaction between the overflow and the corrugation. A set of sixty idealized experiments were conducted with different corrugation geometries and initial conditions. These include changing the aspect ratio of a ridge or a canyon and changing the initial thickness of the overflow, the Coriolis parameter and the density difference between the overflow and the ambient water. Gravity currents are known to exhibit mixing due to nonhydrostatic effects, such as Kelvin–Helmholtz instabilities (Özgökmen et al., 2004; Özgökmen et al., 2006; Özgökmen et al., 2007; Ilıcak et al., 2008b). Complex geometries can increase the amount of mixing by inducing wave breaking and hydraulic jumps (Ilıcak et al., 2009; Ilıcak and Armi, 2010). Large eddy simulations (LES) can be employed to resolve such processes; however LES can be quite expensive computationally. For our problem, in which a relatively large domain is necessary in order to capture the mesoscale eddies, $O(\approx 10^{10})$ grid points would be required for a mixing-resolving resolution of 10 m. Thus, we use the next best thing: an isopycnal high-resolution hydrostatic model which uses a sophisticated mixing scheme. The vertical mixing scheme performs well as long as the shear in the flow is resolved (Jackson et al., 2008). The efficiency of these simulations allows us to carry out a large number of simulations, covering an extensive parameter space. Verification of these results by comparison with a limited number of LES calculations is a subject for future study, but beyond the scope of this paper.

In the control run experiment, the overflow is released without any corrugation in the interior. Analysis of the pathways, transport and mixing of the overflow yields the following conclusions. The flow is in the eddy regime described by Cenedese et al. (2004). We further investigate the frequencies of the tracer field away from the inlet and find out that there are three distinct oscillations; (i) 14 h, (ii) 30 h and (iii) 60 h. These oscillations are barotropic and can also be seen in the velocity field. The same magnitude of oscillations are observed in the Filchner overflow (Darelius et al., 2009). We conclude that the observed fluctuations are due to the eddies generated by the vortex stretching.

We performed twenty-one different experiments with different aspect ratios for each canyon and ridge. The maximum transport of the corrugation was compared to analytic theory (Darelius and Wahlin, 2007). Our idealized simulations show that corrugations steer the plume downslope and ridges are more effective than canyons in transporting the overflow to the deeper ocean. The theory of Darelius and Wahlin (2007) describes that the flow is governed by a single parameter, γ . However, we found that the corrugation Burger number (Bu_c) is a better parameter to describe the flow over topography. Bu_c is a combination of Froude number and the aspect

ratio. Bu_c captures the dependence of overflow-corrugation interaction on the initial overflow thickness, which is not included in γ . The maximum downslope transport of a corrugation can be increased when the height of the corrugation increases (i.e. Bu_c increases) or when the width of the corrugation decreases (i.e. Bu_c increases). The overflow thickness and eastward transport are also computed for different cases. When the overflow encounters a ridge, the gravity currents pile on the upstream side of the ridge and then crosses over the ridge. Increasing the height of the ridge induces a hydraulic jump and strong mixing on the downstream side of the ridge. The entrainment starts to decrease when the height of the corrugation passes a threshold which is around 800 m for the ridges.

A good correlation is found between Bu_c and normalized entrainment rate, E/E_0 . We propose a new parameterization as a function of Bu_c that can be used to represent unresolved shear in coarse resolution models. The new parameterization is an exponential function that increases the shear locally, thus it also increases the turbulent kinetic energy and decreases the gradient Richardson number. We perform three experiments to investigate the performance of the new parameterization. The aim is to reproduce the mixing in the high resolution cases where the corrugations are explicitly resolved. There is a reasonable agreement in the overflow thickness and transport between the models with parameterization and the high resolution models. However, the new parameterization does not yet include an enhanced drag to steer the flow downslope. Such a complex problem is not easily represented by a single universal parameterization. In order to simplify the problem we keep the shape of the corrugation constant, so that the corrugation can be characterized to first-order by the aspect ratio (H/W). A refinement to this characterization could use the corrugation slope instead. Additionally, a single non-dimensional parameter such as the corrugation Burger number may not be sufficient to represent the effects of both mixing and downslope transport due to the presence of a corrugation. Nevertheless, the proposed parameterization is a first step in representing the effects of unresolved corrugations on gravity currents. The information on mixing over a ridge/sill from this study may be used for future improvements and calibration of this parameterization for use in climate models. Overall, we conclude that mixing effects of corrugations can be implemented as unresolved shear in an eddy diffusivity formulation and this parameterization can be used in coarse resolution models.

Appendix A

GOLD has a barotropic and baroclinic time splitting method which allows the 2D barotropic equations are integrated in time faster than the 3D baroclinic equations. Thus, the model uses two types of open boundary conditions; a characteristic method for the barotropic velocities and a radiation boundary condition for the baroclinic velocities. The characteristic boundary condition for the eastern boundary is the following

$$U_{i+1/2}^{n+1} = \frac{1}{2} \left[U^{ext} + U^* + \frac{C_g}{h} (\eta^* - \eta^{ext}) \right], \quad (15)$$

$$\eta_i^{n+1} = \frac{1}{2} \left[\eta^{ext} + \eta^* + \frac{h}{C_g} (U^* - U^{ext}) \right], \quad (16)$$

where $C_g = \sqrt{gh}$ is the group velocity, h is the total depth, U_i^{n+1} and η_i^{n+1} are the new time step barotropic velocity and the surface elevation at the eastern boundary, respectively. Incoming external velocity (U^{ext}) and surface elevation (η^{ext}) can be obtained from a global domain or an analytic function. Outgoing barotropic velocity (U^*) and sea-surface height (η^*) are computed using

$$U^* = cU_{i-1/2}^n + (1 - c)U_{i+1/2}^n, \quad (17)$$

$$\eta^* = \eta_i^n + (0.5 - c)(\eta_i^n - \eta_{i-1}^n), \quad (18)$$

where $c = \Delta t C_g / \Delta x$ is the Courant number. Note that Eq. (18) is slightly different than Eq. (17) since GOLD is a south-west C-grid model, therefore η points are located half-grid space between U points.

The Orlandi-type radiation boundary condition for the baroclinic velocities at the eastern boundary is the following

$$u_{i+1/2}^{n+1} = \frac{u_{i+1/2}^n + c_x^{n+1} u_{i-1/2}^{n+1}}{1 + c_x^{n+1}}, \quad (19)$$

where u is the baroclinic velocity for each layer and c_x is the smoothed group velocity defined as

$$c_x^{n+1} = (1 - \gamma)c_x^n + \gamma \frac{du/dt}{du/dx}, \quad (20)$$

where $\gamma = 0.2$ in this study.

Appendix B

B.1. Cosine-shaped ridge

Darelius and Wahlin (2007) compute that non-dimensional downward transport of a cosine-shaped ridge as

$$T_{c_{ridge}}(\gamma) = \frac{\pi^2}{4} \left[\frac{\pi^2(1 + e^{-\gamma})}{(\pi^2 + \gamma^2)^2} + \frac{\gamma}{2(\pi^2 + \gamma^2)} \right]. \quad (21)$$

B.2. Cosine-shaped canyon

We follow the derivation of the transport of the cosine-shaped canyon in Darelius and Wahlin (2007). Assume that the topography is given by

$$\hat{D}(x, \hat{y}) = sx + \frac{1}{2} [\cos(\pi\hat{y}) + 1], \quad -2 \leq \hat{y} \leq 0. \quad (22)$$

The solution to the overflow thickness in the canyon is given by

$$\hat{h}(\gamma, \hat{y}) = \begin{cases} \frac{\pi^2}{2(\pi^2 + \gamma^2)} [e^{\gamma\hat{y}} - \cos(\pi\hat{y}) - \frac{\gamma}{\pi} \sin(\pi\hat{y})], & Y_L \leq \hat{y} < 0 \\ 0, & \hat{y} < Y_L, \hat{y} > 0 \end{cases}, \quad (23)$$

where $-2 \leq Y_L \leq -1$ and $\hat{h}(Y_L) = 0$. The downward transport cannot be found analytically, thus we computed numerically from

$$T_{c_{canyon}}(\gamma) = - \int_{-\infty}^{\infty} \hat{h} \hat{u} d\hat{y}, \quad (24)$$

where $\hat{u} = \frac{\partial \hat{D}}{\partial \hat{y}} + \frac{\partial \hat{h}}{\partial \hat{y}}$ derived from geostrophy.

Appendix C. Supplementary data

Supplementary data associated with this article can be found, in the online version, at doi:10.1016/j.ocemod.2011.02.004.

References

Adcroft, A., Hallberg, R., Harrison, M., 2008. A finite volume discretization of the pressure gradient force using analytic integration. *Ocean Modell.* 22, 106–113.

Baringer, M.O., Price, J.F., 1997. Mixing and spreading of the mediterranean outflow. *J. Phys. Oceanogr.* 27, 1654–1677.

Blayo, E., Debreau, L., 2005. Revisiting open boundary conditions from the point of view of characteristic variables. *Ocean Modell.* 9, 231–252.

Cenedese, C., Whitehead, J.A., Ascarelli, T.A., Ohiwa, M., 2004. A dense current flowing down a sloping bottom in a rotating fluid. *J. Phys. Oceanogr.* 34, 188–203.

Darelius, E., 2008. Topographic steering of dense overflows: laboratory experiments with V-shaped ridges and canyons. *Deep Sea Res. Part I: Oceanogr. Res.* 55, 1021–1034.

Darelius, E., Smedsrud, L.H., Østerhus, S., Foldvik, A., Gammelsrød, T., 2009. Structure and variability of the Filchner overflow plume. *Tellus Ser. A* 61, 446–464.

Darelius, E., Wahlin, A., 2007. Downward flow of dense water leaning on a submarine ridge. *Deep Sea Res. Part I: Oceanogr. Res.* 54, 1173–1188.

Davies, P.A., Wählin, A.K., Guo, Y., 2006. Laboratory and analytical model studies of the Faroe bank channel deep-water outflow. *J. Phys. Oceanogr.* 36, 1348–1364.

Ezer, T., 2006. Topographic influence on overflow dynamics: idealized numerical simulations and the Faroe bank channel overflow. *J. Geophys. Res.* 111, 2002–+.

Foldvik, A., Gammelsrød, T., Østerhus, S., Fahrbach, E., Rohardt, G., Schröder, M., Nicholls, K.W., Padman, L., Woodgate, R.A., 2004. Ice shelf water overflow and bottom water formation in the southern Weddell Sea. *J. Geophys. Res.* 109, 2015–+.

Gnanadesikan, A., Anderson, W.G., 2009. Ocean water clarity and the ocean general circulation in a coupled climate model. *J. Phys. Oceanogr.* 39, 314–332.

Gordon, A.L., Zambianchi, E., Orsi, A., Visbeck, M., Giulivi, C.F., Whitworth, T., Spezie, G., 2004. Energetics plumes over the western Ross Sea continental slope. *Geophys. Res. Lett.* 31 (21), Art. No. L21302.

Griffies, S.M., Böing, C., Bryan, F.O., Chassignet, E.P., Gerdes, R., Hasumi, H., Hirst, A., Treguier, A.M., Webb, D., 2000. Developments in ocean climate modelling. *Ocean Modell.* 2, 123–192.

Hallberg, R., Adcroft, A., 2009. Reconciling estimates of the free surface height in Lagrangian vertical coordinate ocean models with mode-split time stepping. *Ocean Modell.* 29, 15–26.

Ilıcak, M., Armi, L., 2010. Comparison between a non-hydrostatic numerical model and analytic theory for the two-layer exchange flows. *Ocean Modell.* 35, 264–269.

Ilıcak, M., Özgökmen, T.M., Johns, W.E., 2011. How does the Red sea outflow water interact with Gulf of Aden Eddies? *Ocean Modell.* 36, 133–148.

Ilıcak, M., Özgökmen, T.M., Özsoy, E., Fischer, P.F., 2009. Non-hydrostatic modeling of exchange flows across complex geometries. *Ocean Modell.* 29, 159–175.

Ilıcak, M., Özgökmen, T.M., Peters, H., Baumert, H.Z., Iskandarini, M., 2008a. Performance of two-equation turbulence closures in three-dimensional simulations of the Red sea overflow. *Ocean Modell.* 24, 122–139.

Ilıcak, M., Özgökmen, T.M., Peters, H., Baumert, H.Z., Iskandarini, M., 2008b. Very large eddy simulation of the Red sea overflow. *Ocean Modell.* 20, 183–206.

Jackson, L., Hallberg, R., Legg, S., 2008. A parameterization of shear-driven turbulence for ocean climate models. *J. Phys. Oceanogr.* 38, 1033–+.

Jiang, L., Garwood, R.W., 1998. Effects of topographic steering and ambient stratification on overflows on continental slopes: a model study. *J. Geophys. Res.* 103, 5459–5476.

Johnson, G.C., 2008. Quantifying Antarctic bottom water and North Atlantic deep water volumes. *J. Geophys. Res.* 113, 5027–+.

Legg, S., Hallberg, R.W., Girton, J.B., 2006. Comparison of entrainment in overflows simulated by z-coordinate, isopycnal and non-hydrostatic models. *Ocean Modell.* 11, 69–97.

Macrandar, A., Käse, R.H., Send, U., Valdimarsson, H., Jónsson, S., 2007. Spatial and temporal structure of the Denmark strait overflow revealed by acoustic observations. *Ocean Dyn.* 57, 75–89.

Matsumura, Y., Hasumi, H., 2010. Modeling ice shelf water overflow and bottom water formation in the southern Weddell Sea. *J. Geophys. Res. (Oceans)* 115, 10033–+.

Mauritzen, C., Price, J., Sanford, T., Torres, D., 2005. Circulation and mixing in faroese channels. *Deep Sea Res. Part II* 52, 883–913.

Muench, R., Padman, L., Gordon, A., Orsi, A., 2009a. A dense water outflow from the Ross Sea, Antarctica: Mixing and the contribution of tides. *J. Mar. Syst.* 77, 369–387.

Muench, R.D., Wählin, A.K., Özgökmen, T.M., Hallberg, R., Padman, L., 2009b. Impacts of bottom corrugations on a dense Antarctic outflow: NW Ross Sea. *Geophys. Res. Lett.* 36, 23607–+.

Nof, D., 1983. The translation of isolated cold eddies on a sloping bottom. *Deep Sea Res. Part I: Oceanogr. Res.* 30, 171–182.

Özgökmen, T.M., Fischer, P., 2008. On the role of bottom roughness in overflows. *Ocean Modell.* 20, 336–361.

Özgökmen, T.M., Fischer, P.F., Duan, J., Iliescu, T., 2004. Entrainment in bottom gravity currents over complex topography from three-dimensional nonhydrostatic simulations. *Geophys. Res. Lett.* 31, 13212–+.

Özgökmen, T.M., Fischer, P.F., Johns, W.E., 2006. Product water mass formation by turbulent density currents from a high-order nonhydrostatic spectral element model. *Ocean Modell.* 12, 237–267.

Özgökmen, T.M., Iliescu, T., Fischer, P.F., Srinivasan, A., Duan, J., 2007. Large eddy simulation of stratified mixing in two-dimensional dam-break problem in a rectangular enclosed domain. *Ocean Modell.* 16, 106–140.

Peters, H., Johns, W.E., Bower, A.S., Fratantoni, D.M., 2005. Mixing and entrainment in the red sea outflow plume. part i: Plume structure. *J. Phys. Oceanogr.* 35, 569–583.

Riemschneider, U., Legg, S., 2007. Regional simulations of the Faroe bank channel overflow in a level model. *Ocean Modell.* 17, 93–122.

Sherwin, T., Griffiths, C., Inall, M., Turrell, W., 2008. Quantifying the overflow across the Wyville Thomson ridge into the Rockall trough. *Deep Sea Res. Part I: Oceanogr. Res.* 55, 396–404.

Spall, M.A., Price, J.F., 1998. Mesoscale variability in Denmark strait: The PV outflow hypothesis. *J. Phys. Oceanogr.* 28, 1598–1623.

- Wahlin, A., 2002. Topographic steering of dense currents with application to submarine canyons. *Deep Sea Res. Part 1: Oceanogr. Res.* 49, 305–320.
- Wahlin, A., Darelius, E., Cenedese, C., Lanerhoff, G., 2008. Laboratory observations of enhanced entrainment in dense overflows in the presence of submarine canyons and ridges. *Deep Sea Res. Part 1: Oceanogr. Res.* 55, 737–750.
- Wang, Q., Danilov, S., Schröter, J., 2009. Bottom water formation in the southern Weddell Sea and the influence of submarine ridges: idealized numerical simulations. *Ocean Modell.* 28, 50–59.
- Wilchinsky, A.V., Feltham, D.L., 2009. Numerical Simulation of the Filchner Overflow. *J. Geophys. Res.* 114. 12012–+.